

# Noninvasive Quantification of Contractile Dynamics in Cardiac Cells, Spheroids, and Organs-on-a-Chip Using High-Frequency Ultrasound

Eric M. Strohm,\* Neal I. Callaghan, Yu Ding, Neda Latifi, Naimeh Rafatian, Shunsuke Funakoshi, Ian Fernandes, Cristine J. Reitz, Michelle Di Paola, Anthony O. Gramolini, Milica Radisic, Gordon Keller, Michael C. Kolios, and Craig A. Simmons\*



Cite This: *ACS Nano* 2024, 18, 314–327



Read Online

ACCESS |

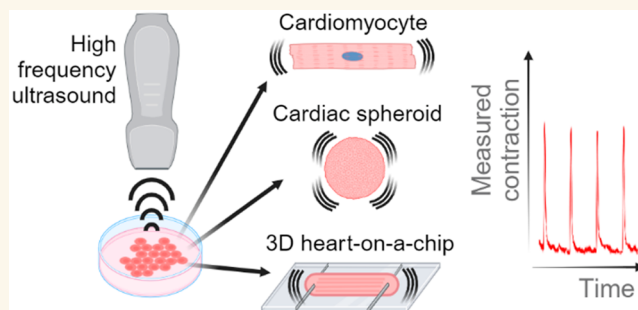
Metrics & More

Article Recommendations

Supporting Information

**ABSTRACT:** Cell-based models that mimic *in vivo* heart physiology are poised to make significant advances in cardiac disease modeling and drug discovery. In these systems, cardiomyocyte (CM) contractility is an important functional metric, but current measurement methods are inaccurate and low-throughput or require complex setups. To address this need, we developed a standalone noninvasive, label-free ultrasound technique operating at 40–200 MHz to measure the contractile kinetics of cardiac models, ranging from single adult CMs to 3D microtissue constructs in standard cell culture formats. The high temporal resolution of 1000 fps resolved the beat profile of single mouse CMs paced at up to 9 Hz, revealing limitations of lower speed optical based measurements to resolve beat kinetics or characterize aberrant beats. Coupling of ultrasound with traction force microscopy enabled the measurement of the CM longitudinal modulus and facile estimation of adult mouse CM contractile forces of  $2.34 \pm 1.40 \mu\text{N}$ , comparable to more complex measurement techniques. Similarly, the beat rate, rhythm, and drug responses of CM spheroid and microtissue models were measured, including in configurations without optical access. In conclusion, ultrasound can be used for the rapid characterization of CM contractile function in a wide range of commonly studied configurations ranging from single cells to 3D tissue constructs using standard well plates and custom microdevices, with applications in cardiac drug discovery and cardiotoxicity evaluation.

**KEYWORDS:** cardiomyocytes, organoids, high-frequency ultrasound, contractility, ultrasound imaging



## INTRODUCTION

Advances in induced pluripotent stem cell (iPSC) technologies have made it possible to create human cardiomyocyte (CM)-based models that mimic key aspects of the *in vivo* structure, function, and physiology of heart tissue in health and disease.<sup>1–7</sup> This has driven significant interest in using 2D and 3D cell-based cardiac models to study and evaluate drug- and stem-cell-based therapies,<sup>8–10</sup> with the opportunity to directly evaluate contractile responses of human cardiac tissues.

However, measurement of contractility to evaluate CM function is not a routine *in vitro* assay. This is due, in part, to the complexity and deficiencies in current contractility measurement systems. The most common contractility tools include impedance plates, multielectrode arrays (MEAs),

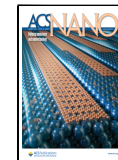
optical imaging methods, and custom techniques that require specialized substrates or methods. Impedance plates and MEAs<sup>11</sup> have good sensitivity and temporal resolution but require specialized substrates containing electrodes, are limited to 2D cultures, and cannot be used on single cells. Further, the measurements can be influenced by differences in confluence levels, cell connectivity, and impulse propagation and cannot

Received: July 10, 2023

Revised: December 17, 2023

Accepted: December 19, 2023

Published: December 26, 2023



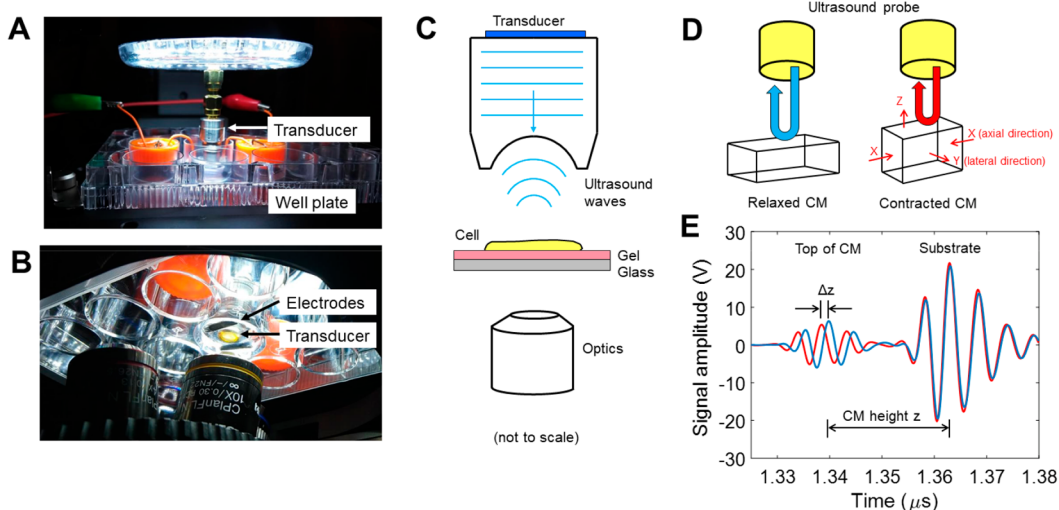


**Figure 1.** (A) Photograph of the imaging system with the ultrasound probe immersed in the well plate. (B) A view from below showing the ultrasound probe between the electrodes. (C) A schematic of the imaging system with the cell located between the ultrasound probe and the optical objective. (D) When a cardiomyocyte (CM) contracts, its length decreases and its height increases. As the CM height increases, the time of propagation of the US wave decreases. (E) The ultrasound waves reflect from the top and bottom of the CM, with the reflections separated in time (blue curve). When the CM contracts and the height increases, the reflection from the top of the CM arrives sooner. The difference in the time of propagation between the relaxed and contracted states gives the change in CM height, while the difference in the time of propagation between the top and bottom of the CM gives the cell height.

provide absolute contraction forces. Optical imaging can provide either high spatial resolution or high temporal resolution but not both when imaging single CMs; clear optical access is also required. Other techniques to measure single-CM contractility—including atomic force microscopy,<sup>12</sup> bending posts,<sup>13</sup> micropost arrays,<sup>14–16</sup> thin film curling<sup>17–19</sup> or wrinkling<sup>20</sup> traction force microscopy (TFM) based on microbead movement,<sup>21,22</sup> and carbon nanotube strain sensors<sup>23</sup>—require specialized components or substrates and significant resources or skills and tend to have low throughput, limiting widespread adoption. Options for assessing the contractility of 3D cardiac tissues are limited to either optical imaging<sup>24</sup> or custom systems such as two-post systems<sup>25–27</sup> including the Biowire II heart-on-a-chip platform.<sup>28</sup>

To address the deficiencies of current contractility measurement systems, we developed a noninvasive, label-free technique to assess the contraction kinetics of CMs and 3D myocardial spheroids and microtissues using high-frequency ultrasound. Clinical ultrasound (<15 MHz) is commonly used in cardiology for probing the heart size and shape, blood perfusion, and myocardial function,<sup>29–31</sup> but does not have the spatial resolution to determine the beat characteristics of single cells and microtissues. As CM models and heart-on-a-chip systems mature and demonstrate advantages over animal models for basic science studies and drug development,<sup>32</sup> versatile tools to measure their contractile dynamics are required. High-frequency ultrasound operating at frequencies over 200 MHz has high spatial resolution (<8 μm) to detect the signals from the top and bottom of a cell to enable evaluation of the mechanical properties at the single-cell level;<sup>33–35</sup> however, limited pulse repetition rates and acquisition speeds have hampered its applications in rapid dynamic processes such as beating CMs. Here we developed a custom acoustic system to track cell and tissue deformation during contraction using ultrasound frequencies from 40 to 200 MHz with capture rates up to 1 kHz. The 10 GS/s sampling rate can track the change in the propagation time of

the ultrasound signals with 0.1 ns precision, translating to better than 100 nm length scales in the ultrasound beam direction. We demonstrate the technique can detect and resolve the contractile profiles of CMs, from single adult mouse cells to 3D cardiac spheroids<sup>36</sup> and microtissues<sup>28</sup> several hundred micrometers in size. Measurements do not require specialized culture platforms or optically clear substrates: here, we demonstrate compatibility with standard polystyrene cell culture plates, porous membrane inserts, and custom heart-on-a-chip devices and measurements from above or below the culture platform. The broad versatility of this high-resolution measurement system makes it an attractive alternative to existing methods to measure CM contractility in basic science, drug screening, and cardiotoxicity studies.

## RESULTS AND DISCUSSION

**Imaging System.** Our custom designed ultrasound system was built on top of a commercial Olympus IX71 microscope to enable simultaneous optical and ultrasound imaging. A 200 MHz single-element ultrasound transducer with a 0.5 mm focal length and an 8 μm spatial resolution was used for imaging single CMs. With a well plate positioned in the microscope, the ultrasound probe was positioned directly over the optical objective for precise positioning under optical guidance (Figure 1A,B). We designed the ultrasound pulse and acquisition hardware to enable rapid, precise pulse transmission and receiving. This was achieved using a high digitization rate of 10 GS/s with a low pulse-pulse jitter of 30 ps. Contraction sequences were recorded at 1000 frames per second, where each frame was an average of a 50-pulse burst cycle performed at a 500 kHz pulse repetition frequency within 0.1 ms, to increase the signal-to-noise ratio (SNR). The entire system was enclosed in an incubator that maintained the temperature at 37 °C for short-term imaging. For longer-term imaging, the ultrasound system is fully compatible with live cell imaging systems with complete environmental control.

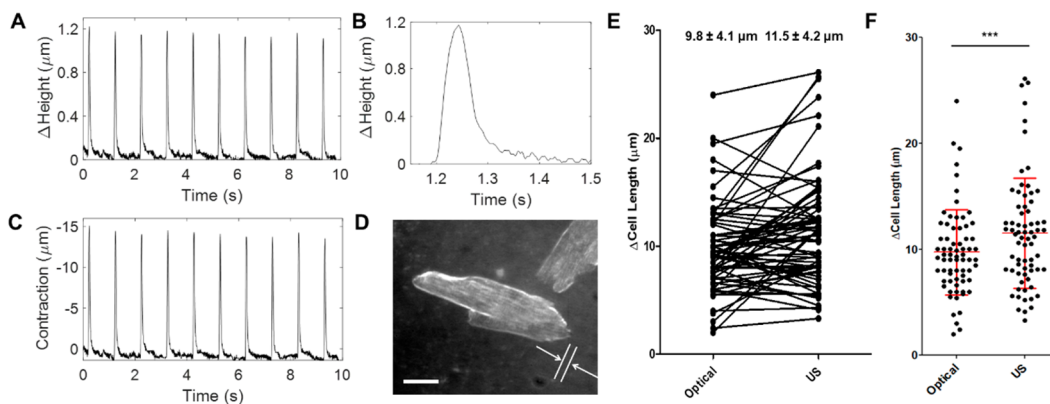


**Figure 2.** (A) The CM beat pattern is found by calculating the change in height throughout the acquisition time. (B) A single beat demonstrating high temporal resolution. (C) The change in CM length (axial contraction), calculated assuming incompressibility and rectangular prismatic geometry. (D) The change in length was found using simultaneous optical imaging (scale bar = 30  $\mu\text{m}$ ). (E) A pairwise and (F) boxplot comparison of the change in length between optical imaging and the ultrasound method (mean  $\pm$  standard deviation, statistically different, \*\*\* $p < 0.001$  by paired  $t$  test).

Cardiomyocytes were isolated from CD1 male mice using previously established methods<sup>37</sup> and then plated onto polyacrylamide gels of 11 kPa stiffness and containing 500 nm fluorescent microbeads in a contraction-inhibiting medium to allow for CM adherence to the gel substrate. The well plate was then transferred to the imaging system, and the medium was replaced with modified Tyrode's solution to enable contractions. Graphite electrodes were placed into the well plate, and the CMs were paced using 25 V/cm, 5 ms duration square pulses at a rate of 1 Hz (S48 Stimulator, Grass Instruments, USA). The ultrasound probe was immersed into the medium and positioned over contracting CMs, and then a 10 s contraction sequence was recorded using both ultrasound (at 1000 fps) and optical imaging (at 20 fps). **Supplementary Video 1** shows the change in the ultrasound signals during CM contraction synchronized with optical imaging. A schematic of the system setup is shown in **Figure 1C**.

As the CMs were insonified with ultrasound waves, some of the wave energy would be reflected from the top of the CM back toward the transducer. The rest of the wave energy would travel through the CM and then reflect from the cell–substrate interface. There was a time delay between these two waves, as the second reflection takes longer to propagate back toward the transducer; the high ultrasound resolution (8  $\mu\text{m}$  lateral and axial) and high sampling rate (10 GS/s) enable capturing the separation of these reflected waves with 100 ps precision (equating to 76 nm in distance in water at 37 °C). The difference in the propagation times between the two reflected waves was used to calculate the CM height. As the CM contracted in the axial direction (i.e., along its long axis), the CM height would increase. As the CM height increased, the propagation time of the ultrasound wave reflected from the top of the CM decreased as it was closer to the transducer, while the propagation time from the bottom of the CM stayed the same (**Figure 1D**). The change in the CM height  $\Delta Z$  was calculated from the change in propagation time  $\Delta t$  from the CM surface using  $\Delta Z = 1/2c^* \Delta t$ , where  $c$  is the sound speed in the medium at 37 °C (1520 m/s). Then, the total CM height  $Z$  was found using the same equation, but with  $\Delta t$  defined as the time delay between the CM top and bottom. This is depicted in **Figure 1E**, where two ultrasound waves are shown: blue indicates the ultrasound waves recorded during relaxation, and red shows peak CM contraction. Optical images (bright-

field or fluorescence) were recorded simultaneously at 20–24 fps (Retiga 2000R, QImaging, USA).

**Ultrasound Measurement of the Contraction of Single Cardiomyocytes.** The beat profile and beat rate can be found by tracking the change in the propagation time of the reflected waves from the CM surface as a function of acquisition time. Acquisition sequences were performed at 1000 fps for a 10 s duration, for a total of 10,000 frames. For each sequence, the change in cell height  $\Delta Z$  for each frame was calculated using the relaxed CM state as a baseline (**Figure 2A**). This high temporal sequencing easily resolves the contraction dynamics and beat profile (**Figure 2B**). These measurements are done in the vertical direction directly above the CM, reflecting the contraction of the CM along its transverse axis. However, axial contraction dynamics along the long axis of the CM are desired. Because adult CMs have rectangular prismatic geometry, are incompressible, and contract uniformly (**Supplemental Video 1**), the change in axial length  $\Delta X$  can be estimated from the change in height  $\Delta Z$  by

$$1 + \frac{\Delta Z}{Z} = \left(1 + \frac{\Delta X}{X}\right)^{-\nu} \quad (1)$$

where  $Z$  is the CM height (measured with ultrasound),  $X$  is the known CM length (determined optically or by ultrasound imaging), and the Poisson's ratio  $\nu = 0.499$ , assuming near-incompressibility. Axial contraction ( $\Delta X$ ) traces (**Figure 2C**) were generated from measurements of  $\Delta Z$  at a single point midway along the length of the cell. We confirmed that  $\Delta Z$  was uniform along the entire length of the CM, with no significant differences between locations, obviating the need for measuring multiple locations per cell and supporting the rectangular geometry model (**Supplemental Figure S1**). We expect this model to be less accurate for CMs with irregular geometry or contraction mechanics, such as immature induced pluripotent stem cell-derived cardiomyocytes (iPSC-CMs).<sup>38</sup> We recorded optical images at 20 fps simultaneously with the ultrasound measurements to compare the calculated length by using ultrasound with the optical measurement (**Figure 2D**). While there was good agreement between the two methods for the majority of the 70 CMs measured (**Figure 2E**), ultrasound yielded significantly greater contraction of some cells (**Figure**

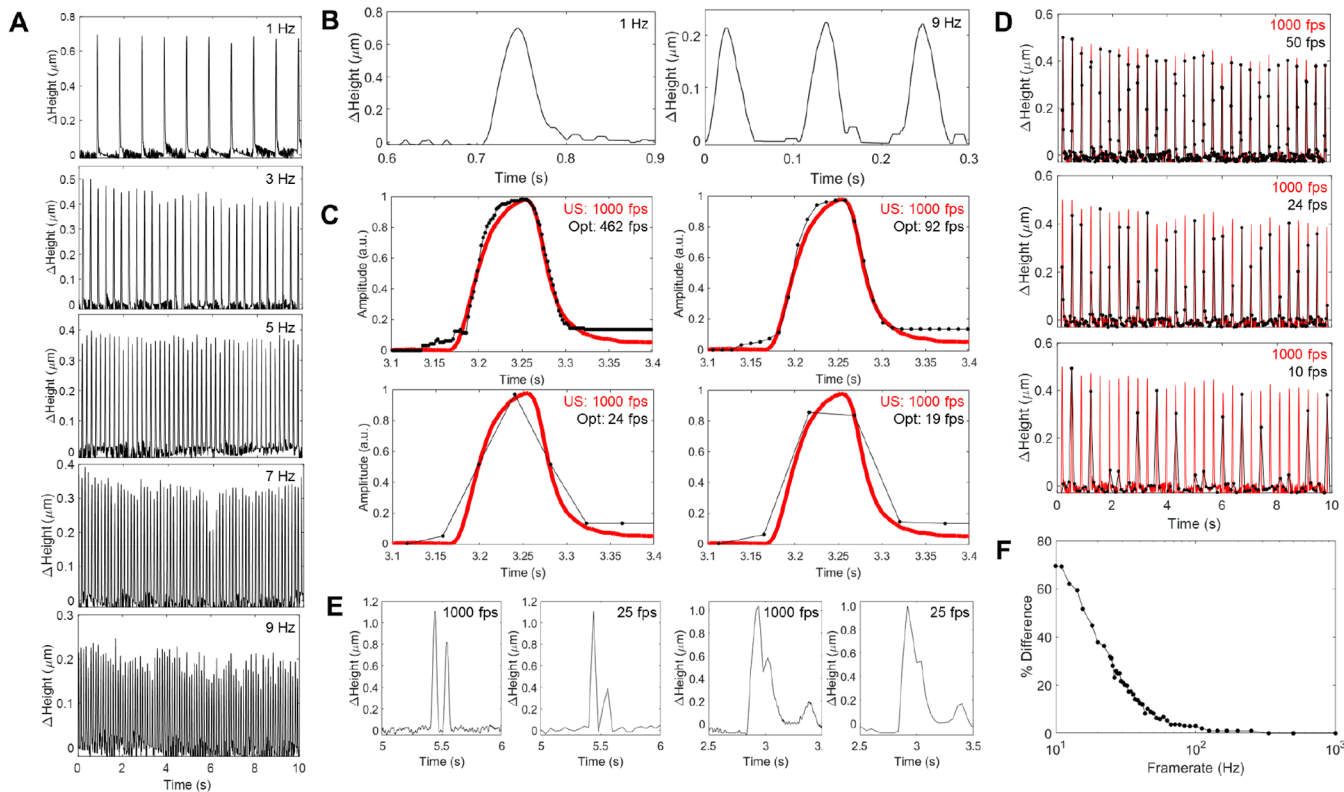


**Figure 3.** (A) The ultrasound system can acquire data at 1000 frames/s, enabling high beat rate temporal resolution for CMs paced at up to 9 Hz. (B) A zoomed-in view of the beat rate at 1 and 9 Hz. (C) A single CM contraction measured simultaneously with ultrasound (at 1000 fps) and optical imaging (at 462 fps) at 1 Hz. The optical frame was decimated to 92, 24, and 19 fps to show how the reduced frame rate distorts the beat pattern and limits the ability to measure the maximum contraction. (D) The 3 Hz plot in (A, red) was decimated to 50, 24, and 10 fps (black) to demonstrate how reduced frame rates can miss the peak contractions. (E) The high frame rate can capture details such as close beats that become obscured when the frame rate is decimated to 25 fps. (F) The difference in peak contraction between 1000 fps and reduced frame rates (8% at 50 fps, 32% at 24 fps, and 69% at 10 fps).

2E) and on average (Figure 2F; optical:  $9.8 \pm 4.1 \mu\text{m}$  vs ultrasound:  $11.5 \pm 5.2 \mu\text{m}$ ;  $p = 0.0007$ ). This discrepancy may be partly due to assumptions inherent in our contraction model (eq 1), including an idealized CM geometry and uniform boundary conditions, but as discussed below, it is likely explained mainly by the insufficient temporal resolution of 20 fps optical imaging that limits fully resolving the peak contractility fully.

To assess the temporal resolution of ultrasound imaging on the contraction measurement, contractions of a single mouse CM were measured when stimulated from 1 to 9 Hz (Figure 3A). As the pacing frequency increased, the change in cell height at peak contraction height decreased, from  $0.7 \mu\text{m}$  at 1 Hz, to  $0.38 \mu\text{m}$  at 5 Hz, and to  $0.2 \mu\text{m}$  at 9 Hz. Figure 3B shows a zoomed image where the beat cycle was 35 ms at 1 Hz and 30 ms at 9 Hz (the beat cycle was measured at the full width at half-maximum). To investigate the effects of the imaging frame rates on the estimation of contractile strain, a CM was measured by using simultaneous ultrasound (at 1000 fps) and optical imaging (at 462 fps) using a uEye high-speed camera (IDS, USA). Despite its higher frame rate, the optical sensitivity was lower and could not be used for fluorescent imaging at experimentally relevant capture rates but was still sufficient to capture the CM edge movement during contraction using brightfield. The change in CM length was tracked using the Manual Tracking ImageJ plugin<sup>39</sup> by advancing through each image frame and manually placing

markers on the CM edge during the contraction. A comparison of the ultrasound vs optical method is shown in Figure 3C. At 462 fps, both the ultrasound and optical methods could clearly resolve the beat profile. This CM was paced at 1 Hz, and the beat cycle lasted about 80 ms. The optical frame rate was decimated to 92 fps, and the beat shape could still be resolved. However, as the frame rate was decimated to 26 and 19 fps, only two data points were acquired during the beat cycle. The beat profile could not be resolved, and more importantly, the maximum contracted value could not be accurately determined. At 26 fps, the optical method measured a peak contraction that was 5–10% lower than the actual value; this discrepancy became more severe at 19 fps.

The effect of the capture frame rate on the beat profile was examined by decimating the ultrasound-acquired beat pattern of the CM paced at 3 Hz from Figure 3A to 50, 24, and 10 fps. Figure 3D compares the original beat pattern captured at 1000 fps (red) to the decimated frame rate (black). At 50 fps, all of the beats were detected, but most were lower in amplitude than at 1000 fps; the average error between the beats measured at 1000 and 50 fps was 8%. At 24 fps, the error in amplitude was 32% and then increased further to 69% at 10 fps. Many beats were missed at 10 fps, and at 24 fps, most beats had only one data point. To illustrate the effect that frame rate has on beat detection, two examples of beats very close together measured at 1000 fps with ultrasound and then decimated to 25 fps are shown in Figure 3E. The lower frame rate introduces

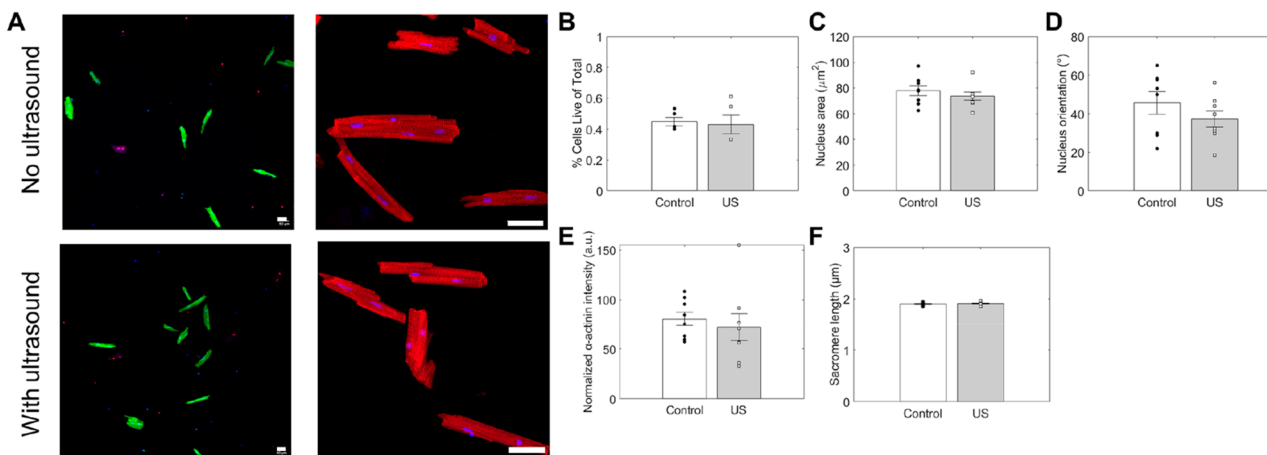


**Figure 4.** (A) Fluorescence micrographs of freshly isolated adult mouse cardiomyocytes in well plates and either outside the ultrasound imaging region (top row; control) or imaged with 200 MHz ultrasound (bottom row, US). Left column shows live (green, calcein AM) and dead (red, ethidium homodimer) cells, with nuclei stained with Hoescht (blue). Right column shows cardiomyocytes stained for  $\alpha$ -actinin (red) and nuclei (blue). Scale bars: 50  $\mu\text{m}$ . (B) Cell viability, (C) nuclear size, (D) nuclear orientation, (E)  $\alpha$ -actinin intensity, or (F) sarcomeric structure were not affected by ultrasound imaging. Data plotted as mean  $\pm$  standard deviation. All comparisons not significant by *t* test ( $p > 0.05$ ).

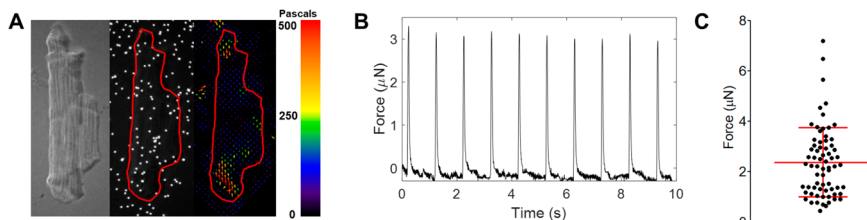


**Figure 5.** (A) Traction force microscopy (TFM) was used to determine the force of contraction of the beating CMs. The CM axial elastic modulus was estimated from the force measured by TFM, and strain and cross-sectional area were measured by ultrasound. (B) A typical contraction force curve for a CM, based on the axial elastic modulus estimate and contractility measured by ultrasound. (C) 70 CMs were measured using this technique with an average force of contraction of  $2.34 \pm 1.40 \mu\text{N}$  (mean  $\pm$  standard deviation).

errors in the beat shape, beat pattern, and beat separation, and in the second example, the second beat is nearly consumed within the first beat. The error between 1000 fps and lower frame rates is shown in Figure 3F. The error in beat amplitude was less than 4% when frame rates above 66 fps were used and less than 9% when frame rates above 42 fps were used. Significant errors were observed below 25 fps, where the error was greater than 25%. Comparing the CM length measurements using 20 fps optical imaging to 1000 fps ultrasound imaging (Figure 2F), only 24% of the optical measurements were within 10% of the ultrasound values. The significant underestimation of peak contraction with low frame rate optical imaging is consistent with our single-cell observations (Figure 2E) and explains the observed discrepancies with ultrasound measurements (Figure 2F). The insight provided by the high-resolution ultrasound measurements informs specifications for lower resolution methods: frame rates above 30 fps should be used to ensure beats are not missed, and frame rates above 66 fps are needed for accurately resolved beat profiles. Optical imaging at these frame rates is achievable with specialized cameras, but it is notable that standard frame rate cameras (<40 fps) are commonly used for CM studies.<sup>40–45</sup> MEA systems also do not match the temporal resolution of our ultrasound system and cannot detect movement irregularities that can occur in arrhythmias or other disorders. However, as ultrasound imaging can be done

without optical access, it could be combined with MEAs for simultaneous measurement of CM electrophysiology and contraction kinetics with high resolution.

**Effect of High-Frequency Ultrasound on Single-Cardiomyocyte Viability and Subcellular Structure.** To confirm that 200 MHz contraction imaging was noninvasive to single CMs, we compared the viability and nuclear and cytoskeletal structure of single adult mouse CMs subjected to ultrasound to those in the same culture well, but outside the imaging field. We observed no differences in CM viability (Figure 4A,B), nuclear size (Figure 4C) or orientation (Figure 4D),  $\alpha$ -actinin intensity (Figure 4E), or sarcomere length (Figure 4A,F). These data confirm that CM viability and subcellular structure were not affected by 200 MHz ultrasound imaging, consistent with previous studies that found no effect of high-frequency (10–400 MHz) ultrasound on cell viability at standard imaging pressures.<sup>46–49</sup>

**Ultrasound-Based Estimation of Contractile Force by Single Cardiomyocytes.** In addition to measuring the beat rate, rhythm, and contraction strain, the force of contraction is a useful CM functional metric. The force of contraction,  $F$ , is often estimated from the contraction strain assuming linear elasticity according to

$$F = E_x \varepsilon_x A \quad (2)$$

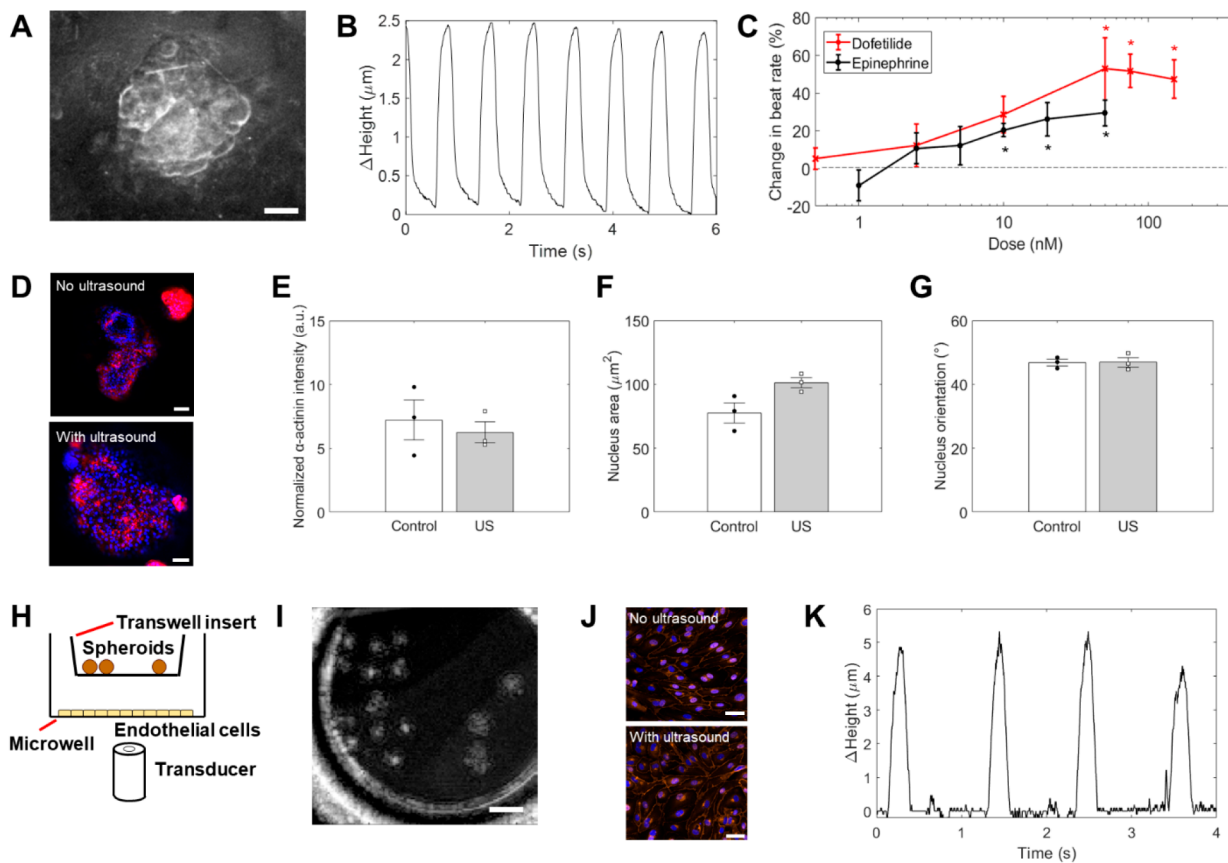


**Figure 6.** (A) A representative cardiac spheroid 200  $\mu\text{m}$  in diameter was measured using 80 MHz ultrasound (scale bar = 50  $\mu\text{m}$ ), with the (B) beat pattern obtained using ultrasound. (C) Drug dose curves measured by ultrasound on cardiac spheroids treated with epinephrine ( $n = 4$  spheroids, black line) or dofetilide ( $n = 5$ , red line). Dashed line denotes untreated control. In both cases, the beat rate increased with dose. Data plotted as mean  $\pm$  standard deviation; \* $p < 0.05$  relative to untreated control. In (D) cardiac spheroids not imaged (top image) or imaged with ultrasound (bottom) (scale bar = 50  $\mu\text{m}$ ), there was no difference in (E)  $\alpha$ -actinin intensity, (F) nuclear size, or (G) nuclear orientation. Data plotted as mean  $\pm$  standard deviation; all comparisons not significant,  $p > 0.05$ . (H) Schematic of cardiac spheroid–endothelial cell coculture, using a Transwell insert and imaged by ultrasound below the well plate. (I) Ultrasound image scan of several spheroids imaged through the micowell, endothelial monolayer, and porous membrane of the Transwell insert. Scale bar: 1 mm. (J) Endothelial cells were unaffected by ultrasound imaging, with no differences in viability, confluence, or morphology between control (top) and ultrasound-imaged (bottom) cultures (VE-cadherin in orange and nuclei in blue). Scale bar = 50  $\mu\text{m}$ . (K) Representative beat pattern of a cardiac spheroid measured in the coculture setup with imaging from below.

where  $\varepsilon_x$  is the axial strain,  $A$  is the cross-sectional area of the CM, and  $E_x$  is the elastic modulus in the axial direction. While strain and area can be determined by the ultrasound method described here, the elastic modulus cannot. CMs have anisotropic mechanical properties, owing to their elongated geometry with sarcomeres and other structures positioned along the length of the cell.<sup>50–53</sup> Nanoindentation techniques like atomic force microscopy (AFM) can be used to measure cell stiffness but typically assume isotropic properties, and for cardiomyocytes, typically measure the transverse elastic modulus based on measurement perpendicular to the axis of contraction, not the axial elastic modulus. To our knowledge, the only measurements of the axial elastic modulus of live CMs have been done on rat CMs subjected to tensile stretch, yielding equivalent moduli of  $\sim 12$  kPa, which was about six times stiffer than the transverse elastic modulus.<sup>54</sup> However, these measurements may not reflect the moduli of a CM contracting auxotonically, which is arguably more physiological. To make those measurements with high temporal resolution, we combined the ultrasound method with traction force microscopy. TFM is a gold standard method to measure

the contraction force of CMs cultured on soft gels embedded with nanoscale fluorescent beads that shift locally as a CM contracts (Figure 5A). The force exerted upon the gel by the CM can be calculated using the Fourier transform traction cytometry (FTTC) method,<sup>55,56</sup> based on the elastic modulus of the gel. Combined ultrasound–TFM measurements yielded the force (via TFM), strain (via ultrasound), and cross-sectional area (width via optical or ultrasound imaging and height via ultrasound), from which the axial elastic modulus was estimated by eq 2. For adult mouse CMs, we determined  $E_x = 46 \pm 12$  kPa, which was greater than that measured by Caporizzo et al.,<sup>54</sup> ostensibly reflecting differences in constrained vs physiologically contracting CMs. Notably, we determined the transverse elastic modulus of single adult mouse CMs measured by AFM nanoindentation ( $10.1 \pm 2.2$  kPa) to be 4.6-fold less than the axial modulus, as expected and consistent with previous measurements.<sup>54</sup> The mean axial modulus was then used to calculate the contraction force of CMs that were measured using only ultrasound. A representative plot of the force vs time is shown in Figure 5B. In this example, the beat-to-beat peak force varied from

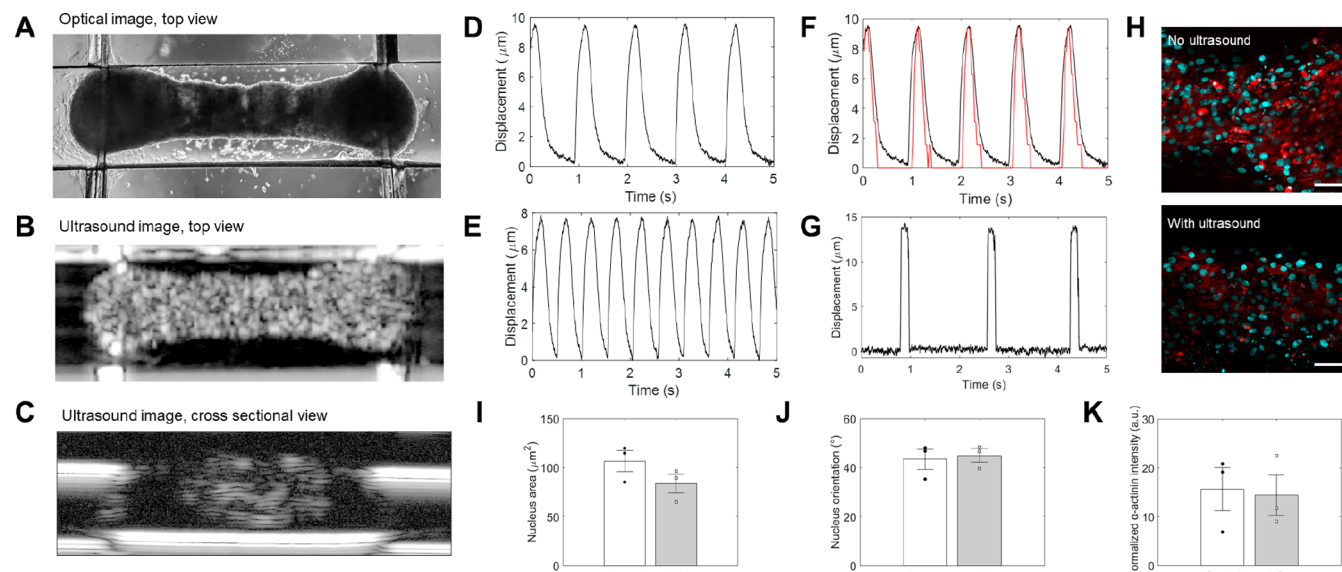


**Figure 7.** (A) Optical image of the Biowire II 3D cardiac microtissue. (B) Top and (C) cross-sectional views of the Biowire II using 40 MHz ultrasound. (D) Ultrasound-measured beat pattern of the Biowire II stimulated at 1 Hz and (E) at 2 Hz. (F) A comparison of the beat pattern of the Biowire II stimulated at 1 Hz using ultrasound (black) and optical tracking of the bending post (red). (G) Ultrasound-measured beat pattern of a Biowire II measured from underneath the sample through the well plate and microdevice. (H) Comparison of cardiomyocytes in control microtissues (top) and those imaged with ultrasound (bottom) (scale bar = 50  $\mu$ m) showed no differences in the (I) nuclear area, (J) nuclear orientation, or (K)  $\alpha$ -actinin intensity. Data plotted as mean  $\pm$  standard deviation; all comparisons not significant,  $p > 0.05$ .

2.96 to 3.30  $\mu$ N, with an average value of  $3.10 \pm 0.10 \mu$ N. This was repeated for 70 CMs, with an average force of  $2.34 \pm 1.40 \mu$ N (Figure 5C). These values, obtained for cells on standard culture substrates, are similar to what others have reported for adult mouse CMs using specialized culture formats and devices: 1.8  $\mu$ N using traction force microscopy,<sup>57</sup> 5.8  $\mu$ N using a micro-electromechanical systems (MEMS) force gauge,<sup>58</sup> 2–8  $\mu$ N using a micro force gauge,<sup>59</sup> 0.5–2  $\mu$ N using a carbon fiber force-length control system,<sup>60</sup> and 10  $\mu$ N using magnetic bead movement.<sup>61</sup>

While we found good correspondence with previous contraction force measurements in single CMs, there are clear limitations to our approach. While assumptions of anisotropic linear elasticity are often sufficient for *in vitro* CM models used for disease modeling or drug testing, CMs and cardiac microtissues have nonlinear viscoelastic properties that are not captured with our model. In theory, the high temporal resolution of US imaging coupled with TFM would enable force-deformation relationships of auxotonically beating adult CMs to be measured with sub-single-contraction resolution, from which nonlinear stress-strain relationships could be generated. This would require TFM imaging at higher frame rates and higher sensitivity than that performed in this study. Our current approach is unable to measure the viscous properties of beating CMs, as such measurement requires complex setups that perturb cells (e.g., ref 54), which we intentionally avoided, as our intended applications necessitate noninvasive measurements. More fundamentally, our current method is unable to measure cell-specific material properties, with the force estimates necessarily based on population means; the same applies to optical contraction imaging. However, high-frequency ultrasound may have advantages in addressing this limitation, as the system could be adapted for high-resolution shear wave viscoelastography<sup>62–64</sup> to measure

the cell and tissue viscoelastic properties needed for direct contraction force calculation.

**Ultrasound Measurement of the Contraction Kinetics of 3D Cardiac Spheroids and Spheroid–Endothelial Cell Cocultures.** A significant advantage of the ultrasound system is that it can examine different length scales, from single cells to mm-sized microtissue samples by changing the ultrasound frequency. 3D cardiac spheroids<sup>36</sup> 100–300  $\mu$ m in diameter were examined using an 80 MHz ultrasound transducer, which had a 6 mm focal length, 25  $\mu$ m resolution in the z-axis (direction of propagation (or) transverse CM direction) and 60  $\mu$ m resolution in the x-axis (perpendicular to the axis of propagation (or) or axial CM direction). The same measurement procedure described for the single CMs was used; the transducer was positioned above the spheroid, and ultrasound signals were acquired for 6 s. A representative optical image of the spheroid and corresponding ultrasound-acquired beat profile are shown in Figure 6A,B. The force calculation for the spheroids presents an additional difficulty, as the spheroids are irregularly organized (Supplementary Video 2) and, in contrast to single CMs, cannot be accurately modeled using an idealized geometry to estimate contractile force reliably. However, contractility can be measured with high temporal resolution to determine the beat rate and rhythm, which are important metrics for evaluating drug response. To demonstrate this, we performed a drug-dose curve using epinephrine (1–50 nM) and dofetilide (0.5–150 nM). As expected, the beat rate increased steadily with epinephrine treatment with a final beat rate increase of 29% above baseline at 150 nM (Figure 6C). Similarly, for dofetilide, the beat rate increased steadily to peak at 53% above the baseline at 50 nM (Figure 6C). Importantly, we observed no detrimental effect of 80 MHz ultrasound on  $\alpha$ -actinin expression (Figure 6D,E) or

nuclear structure or alignment (Figure 6D,F,G) of CMs in the spheroids.

In contrast to standard optical imaging, our ultrasound method allows imaging through the volume of 3D tissue. To demonstrate the insights this can provide, we compared ultrasound signals from mature vs. less mature cardiac spheroids. Ultrasound signals from mature cardiac spheroids demonstrated synchronous beating throughout their thickness, suggestive of mature, well-connected cardiomyocytes with fast electrical transmission (Supplemental Video 2). Contraction was typical of nearly incompressible tissues, with the top surface of the spheroid moving up (toward the transducer in this case) and the bottom surface moving down (away from the transducer) as the spheroid contracted laterally. In contrast, ultrasound signals from less mature spheroids showed asynchronous contraction through the spheroid thickness with no clear contraction pattern (Supplemental Video 3). These through-thickness features, which are not visible optically, are consistent with less dense spheroids with immature, poorly connected cardiomyocytes. Thus, beyond imaging spheroid contraction, the 3D imaging capabilities of the ultrasound method can detect functional differences reflective of spheroid maturity and the associated 3D microstructure.

Finally, we tested if ultrasound was capable of imaging beat kinetics of cardiac spheroids in Transwell inserts cocultured with a monolayer of cardiac endothelial cells on the bottom of a well plate (Figure 6H). Because of the endothelial layer, imaging distance, and light diffraction by the Transwell track-etched porous membrane, optical imaging of the spheroids with an inverted microscope is not possible in this setup. However, with an inverted configuration of the ultrasound probe (i.e., the transducer below the well plate to avoid having to place the probe in the culture medium) (Figure 6H), we were able to visualize the spheroids through the plastic substrate, endothelial layer, and porous membrane with a 40 MHz probe (Figure 6I). As with the spheroids, we detected no change in the endothelium subjected to ultrasound (Figure 6J). As expected with the lower frequency probe and intervening substrates, the signal from the spheroids was noisier than with an upright 80 MHz probe but was still sufficient to measure the spontaneous beat kinetics of the spheroids (Figure 6K).

**Ultrasound Measurement of the Contraction Kinetics of 3D Cardiac Microtissues.** The ultrasound system was then evaluated using the Biowire II, a 3D microtissue platform used to mature cardiac tissues and evaluate drug toxicity.<sup>65</sup> In this system, iPSC-CMs are suspended between two wires, which deflect when the CMs contract (Figure 7A). The deflection is measured optically to determine the beat rate and force of contraction. Using a 40 MHz ultrasound probe, the Biowire was scanned from above to create an overhead view (ultrasound C-scan) (Figure 7B) and a cross-sectional view through the center (ultrasound B-scan) to determine the Biowire shape and dimensions (Figure 7C). The ultrasound probe was then positioned over the middle of the Biowire, and ultrasound measurements were performed using stimulation at 1 and 2 Hz, using the sample procedure as with single CMs. The ultrasound technique could detect the top and bottom of the Biowire, but in contrast to single CMs, no change in tissue thickness was detected with axial contraction (Supplemental Video 4). The observation that the microtissue cross-section did not change despite a reduction in length suggests that the extracellular matrix in the engineered microtissues compacted under contraction; tissue compaction is commonly observed

with other contractile cells (e.g., fibroblasts) in fibrous matrices.<sup>66</sup> Also notable was that the ultrasound signal in the middle of the tissues was lower than that on the periphery, indicating less scattering in the core (Supplemental Video 4). Less scattering in engineered tissues correlates with lower cell densities,<sup>67</sup> indicating reduced cellularity in the core of the microtissues relative to the periphery. Indeed, reduced cellularity is often observed in the core of thick microtissues,<sup>68</sup> including the Biowires used here (Supplemental Figure 2), and may facilitate compaction of the microtissues under contraction by the cells on the periphery.

Regardless, the movement measured by ultrasound was sufficient to determine the beat rate and profile, which was similar to that of the CM spheroids, with rapid shortening and a slightly slower relaxation when stimulated at 1 or 2 Hz (Figure 7D,E). Of note, while the beat rates determined by ultrasound and 20 fps optical imaging were identical, the temporal resolution of the standard optical method was too low to resolve the fine details of the beat profile that were observed with ultrasound when imaged from directly above the Biowire (Figure 7F). We also imaged the microtissue with the 40 MHz probe *below* the well plate, which would be important for microdevices without optical access to visualize the tissue and to more easily maintain sterile cultures. Imaging through the plastic substrates of the well plate and heart-on-a-chip platform decreased the signal-to-noise ratio of the ultrasound signal, but it was still sufficient to measure beat rate, comparably to optical methods (Figure 7G). As with the single CMs and cardiac spheroids, the CMs in the Biowire microtissues were unaffected by 40 MHz imaging, including  $\alpha$ -actinin expression (Figure 7H,I) or nuclear structure or alignment (Figure 7H,K,L).

## STUDY LIMITATIONS

While high-frequency ultrasound is an attractive alternative to optical and specialized methods for the characterization of CM contractile function, it does have limitations. In particular, optical imaging has the potential to achieve a similar performance of single CM contraction measurement in standard 2D culture, with ultrasound's main advantage being measurement when optical access is unavailable (e.g., on multielectrode arrays). Further, our single CM contraction model assumes regular geometry; while we showed that this was valid for adult CMs, it may not be for cells with irregular geometry and contraction patterns (optical measurement suffers in these cases as well). Similar to optical methods, direct measurement of contractile force is not possible with the current ultrasound method and still requires specialized methods (e.g., TFM for 2D cultures or postdeflection for 3D microtissues). Further development of high-frequency ultrasound to enable shear wave viscoelastography of cells or microtissues would address this limitation. Finally, high-frequency ultrasound signals can be attenuated when imaging from below the tissue cultures through the base of a polystyrene well plate. Despite this limitation, signal quality was sufficient in this inverted configuration to resolve spheroid and microtissue contractile dynamics, including *through* the tissue volume, which is a significant advantage over current methods.

## CONCLUSION

The ultrasound system detailed here represents a noninvasive, nondestructive, and label-free means by which to characterize cardiac cell or tissue contractility and mechanics *in vitro*. It is highly versatile and applicable to various culture formats and spatial scales, from single cells to complex 3D microtissues. Furthermore, this technique could be multiplexed in real time with other *in situ* monitoring (e.g.,  $\text{Ca}^{2+}$  or voltage fluorescence imaging) or even complexed with optically opaque modalities (e.g., multielectrode arrays) for high-yield physiological experimentation. By providing insights into myocardial contractile kinetics and beat profile, this system may allow for enhanced characterization of the mechanical aspects of pathophysiology and drug responses, therefore contributing to higher-value *in vitro* experimentation, personalized medicine, and drug screening applications.

## MATERIALS AND METHODS

**Cardiomyocyte Culture.** Primary adult cardiomyocytes were isolated by previously established methods from 8 week old CD1 male mice.<sup>37</sup> Cells were plated onto 250  $\mu\text{m}$  thick, 11 kPa polyacrylamide gels as described previously,<sup>57</sup> except that Geltrex was mixed into the prepolymerized gel solution at a final concentration of 16.7%. Gels were cast onto 18 mm round (3-aminopropyl)triethoxysilane (APTES)-functionalized glass coverslips and embedded with 500 nm fluorescent nanobeads on their top surface. To inhibit contractions, cells were incubated with Tyrode's solution with 15  $\mu\text{mol/L}$  blebbistatin (Toronto Research Chemicals, Canada).<sup>57</sup> Prior to measurements, cells were induced to contract spontaneously using sterile modified Tyrode's solution containing (in mmol/L) NaCl (130), KCl (5),  $\text{NaH}_2\text{PO}_4$  (0.5), D-glucose (10), (4-(2-hydroxyethyl)-1-piperazineethanesulfonic acid) (HEPES) (10), taurine (10),  $\text{MgSO}_4$  (1), and  $\text{CaCl}_2$  (1.8), pH 7.4, as well as 1× chemically defined lipid concentrate (11905031, Gibco/Thermo Fisher Scientific). In the experiments aimed at determining the effect of ultrasound imaging on cell function, adult CMs were grown in Petri dishes coated with Matrigel. Cells within the ultrasound imaging area in the centers of the dishes were compared to nontreated control cells outside the imaging area.

**Biowire Fabrication and Culture.** Myocytes were differentiated from the human induced pluripotent stem cell (hiPSC) line BJD1 (gift from Dr. William Stanford, now at Ottawa Hospital Research Institute) following established monolayer differentiation protocols.<sup>69,70</sup> Dissociated hiPSC-derived myocytes were mixed with human cardiac fibroblasts (Lonza, NHCF-V) in a ratio of 9:1. The cell mixture was resuspended in a collagen/Matrigel-based hydrogel at the concentration of 3 mg/mL and 150  $\mu\text{L}/\text{mL}$ , respectively. The hydrogel containing cells was then seeded in the Biowire II platform.<sup>65</sup> Throughout the first week of culture, the microtissue compacted and formed around the wires, suspending the microtissue, after which the microtissues were imaged. For experiments aimed at determining the effect of ultrasound on the function of CMs in the microtissues, Biowires subjected to ultrasound imaging along their length were compared to control Biowires, not subjected to ultrasound imaging.

**Spheroid Fabrication and Culture.** For ventricular cardiomyocyte differentiation for cardiac spheroids, a modified version of the embryoid body (EB)-based protocol was followed.<sup>71</sup> hPSC populations (HES2) were dissociated into single cells (TrypLE, ThermoFisher) and reaggregated to form EBs in StemPro-34 media (ThermoFisher) containing penicillin/streptomycin (1%, ThermoFisher), L-glutamine (2 mM, ThermoFisher), transferrin (150 mg/mL, ROCHE), ascorbic acid (50 mg/mL, Sigma), monothioglycerol (50 mg/mL, Sigma), ROCK inhibitor Y-27632 (10 uM, TOCRIS), and rhBMP4 (1 ng/mL, R&D) for 18 h on an orbital shaker (70 rpm). On day 1, the EBs were transferred to mesoderm induction media consisting of StemPro-34 with the above supplements,

excluding ROCK inhibitor Y-27632 and rhBMP4 (8 ng/mL), rhActivinA (12 ng/mL, R&D), and rhbFGF (5 ng/mL, R&D). On day 3, the EBs were harvested, dissociated into single cells (TrypLE), and reaggregated in cardiac mesoderm specification media consisting of StemPro-34, the Wnt inhibitor IWP2 (2  $\mu\text{M}$ , TOCRIS), and rhVEGF (10 ng/mL, R&D). On day 5, the EBs were transferred to StemPro-34 with rhVEGF (5 ng/mL) for another 5 days and then to DMEM high glucose (4.5 g/L, ThermoFisher) media with compaction factors CHIR (1  $\mu\text{M}$ , TOCRIS), IGF2 (25 ng/mL, R&D), and human insulin (10 ng/mL, Sigma) at day 10 for another 6 days. From day 16 to day 18, the EBs were transferred to DMEM high glucose media with XAV (4  $\mu\text{M}$ , TOCRIS) and then transferred to maturation media [DMEM containing low glucose (2 g/L) with palmitic acid (200  $\mu\text{M}$ , Sigma), dexamethasone (100 ng/mL, Bioshop), T3 hormone (4 nM, Sigma), and GW7647 (PPARA agonist, 1  $\mu\text{M}$ , Sigma)] for the following 9 days. Finally, the EBs were cultured in DMEM containing low glucose supplemented with palmitic acid (200  $\mu\text{M}$ ) alone for the following 5 days (a total of 32 days). Cultures were incubated in a low-oxygen environment (5%  $\text{CO}_2$ , 5%  $\text{O}_2$ , 90%  $\text{N}_2$ ) for the first 10 days and a normoxic environment (5%  $\text{CO}_2$ , 20%  $\text{O}_2$ ) for the following 22 days. From day 10 to day 32, the EBs were cultured in polyheme-coated low-binding 10 cm culture dishes on an orbital shaker (70 rpm). For drug response experiments, cardiac spheroids ( $N = 4\text{--}5/\text{condition}$ ) were treated with epinephrine (1–50 nM), dofetilide (0.5–150 nM), or vehicle controls for 3 min. Beat rate was measured using an 80 MHz ultrasound transducer. For coculture experiments, cardiac microvascular endothelial cells (Lonza, USA; cat# CC-7030) were grown on tissue-culture-treated polystyrene 12-well microplates in supplemented EGM-2 medium (Lonza, USA; cat# CC-3202). Once confluent, Transwell inserts containing cardiac spheroids were transferred to the endothelial cultures ( $N = 3$  independent cultures) for imaging from below the well plate with a 40 MHz ultrasound transducer. For experiments aimed at determining the effect of ultrasound on the function of CMs in the spheroids, spheroids were imaged within culture dishes. Spheroids within the ultrasound imaging area in the centers of the dishes were compared to nontreated control cells outside the imaging area.

**Ultrasound System.** A custom ultrasound system was designed and built to rapidly insonify and acquire ultrasound signals with high precision. An Intel i7 computer with a trigger card (Spincore, USA) was used to control the hardware. A pulse generator (Geozondas, Lithuania) generated monocycle pulses that were sent through an RF-switch (Mini-Circuits, USA) to an ultrasound transducer (200 MHz transducer for single CMs, 80 MHz transducer for the cardiac spheroids, and 40 MHz for the Biowires). Returning signals were amplified by a 30 dB amplifier (Miteq, USA) before digitization at 10 GS/s with a 14-bit resolution (Teledyne SP Devices, Sweden). Cells were insonified at 1000 samples/s, where each sample was the average of a 50-pulse burst with a 500 kHz pulse repetition frequency. The 50-pulse burst was used to increase the SNR and occurred within 0.1 ms; we assumed that there was negligible cell movement during this time. Time-gating was used to eliminate unwanted signals due to reverberations and interference, e.g., from imaging through plastic substrates. A 3-axis stage (Thorlabs, USA) was mounted to an Olympus IX71 microscope stage to move the ultrasound transducer over each individual cell under optical guidance (Figure 1). The angle of the transducer was adjustable with set screws to ensure that it was perpendicular to the bottom of the culture substrate, as determined by the transducer position that gave the highest pulse echo signal from the substrate. A total of 10,000 frames (10 s acquisition time) were then acquired with simultaneous optical video using a QImaging Retiga 2000 at 20–24 fps or an IDS UI-3140CP high-speed camera at 462 fps. The entire microscope system was enclosed in a temperature-controlled incubator with a temperature set point of 37 °C (In Vivo Scientific, USA).

**Contraction Measurements and Force Estimates.** CM contraction was determined by relating the change in the height of the CM during each contraction (measured using ultrasound) to an axial deformation by assuming a rectangular prism geometry and

uniform, incompressible contraction (eq 1). First, the baseline propagation time of the ultrasound echo from the cell surface at relaxation (e.g., 1.340  $\mu$ s in Figure 1E) was found. As the CM contracts, the cell height increases (e.g., to 1.339  $\mu$ s in Figure 1E); the change in CM height was calculated for each frame using the equation

$$\Delta Z = \frac{1}{2}c\Delta t \quad (3)$$

where  $c$  is the sound speed in the liquid (1520 m/s) and  $\Delta t$  is the difference in propagation time between the baseline relaxation time and the signal at each frame. The transverse strain  $\epsilon_z = \Delta Z/Z$  was calculated using the change in cell height  $\Delta Z$  and cell height  $Z$ , measured at relaxation. The axial strain  $\epsilon_x$  in the direction of contraction was then calculated using Poisson's ratio  $\nu = -d\epsilon_x/d\epsilon_z$ , where  $\nu = 0.499$  for a nearly incompressible cell, assuming rectangular prism geometry (eq 1). The axial stress  $\sigma_x$  was then calculated using the linear elastic equation

$$\sigma_x = E_x \epsilon_x \quad (4)$$

where  $E_x$  is the axial elastic modulus. This equation assumes that the CM is a homogeneous, incompressible, and elastic material. The longitudinal force exerted by the cell was then calculated using

$$F_x = \sigma_x A \quad (5)$$

where  $A$  is the cross-sectional area of the cell, with the cell width obtained through optical imaging and the cell height obtained through ultrasound. These calculations were performed for every successive signal acquired, resulting in plots of  $\Delta$ height,  $\Delta$ length, and force measurements vs time.

**Contractile Force Measurement Using Traction Force Microscopy.** Fluorescent polystyrene microbeads 500 nm in diameter (Polysciences Inc., USA) were embedded in polyacrylamide gels with a stiffness of 11 kPa. Videos of beating CMs and the fluorescent beads were acquired at a frame rate of 20–24 fps using an Olympus IX71 microscope with a QImaging Retiga 2000 CCD camera and Micromanager 1.4.<sup>72</sup> The displacement field was measured by tracking the motion of the fluorescent beads. An iterative particle image velocimetry (PIV) method was used, where the image was divided into increasingly smaller interrogation windows to determine the displacement vectors. The traction field was then calculated using the FTTC method using ImageJ plugins.<sup>55,56</sup> FTTC-determined stresses were integrated within the cell area to give a total cell force scalar, given the assumptions of uniaxial contraction and zero vector sum.<sup>38</sup>

**Atomic Force Microscopy.** A JPK atomic force microscope (Bruker JPK NanoWizard 4, Cambridge, UK) was used to determine the elastic modulus of the polyacrylamide gels and the elastic modulus of nonbeating adult CMs in the transverse direction. The indentation tests were performed using force spectroscopy in contact mode at room temperature. Tipless silicon nitride AFM cantilevers (Bruker, MLCT-O10, cantilever D with a nominal spring constant of 0.03 N/m) were functionalized using 10  $\mu$ m radius spherical polystyrene beads (Phosphorex Inc., Hopkinton, MA, USA). A contact-based thermal tuning method was applied to determine the precise spring constants. Each hydrogel sample was indented in three locations composed of a 10  $\mu$ m  $\times$  10  $\mu$ m area, in which four points were indented. The indentation tests were repeated five times at every indentation point, i.e., five technical replicates per point. For the adult CMs, cells were indented at three locations in their center and at three locations at the cell end. Force–deflection curves were recorded, and the elastic modulus was obtained from the extended curves using the Hertz/Sneddon model. Data analysis was performed using JPK Data Processing software (version 6.3.11). CM cells and tissues are strongly anisotropic.<sup>51–53</sup> AFM measurements yield the elastic modulus of the CMs along the transverse direction, perpendicular to the axis of contraction, while our linear elastic eq 4 requires axial stiffness, which is unknown for single contracting CMs. Finally, the elastic modulus may be a dynamic parameter that changes during contraction. For these reasons, we decided to use an experimentally extracted elastic

modulus that was calculated by using a combined ultrasound-TFM method. Equations 4 and 5 were combined and isolated to solve for  $E$ ,

$$E = \frac{F}{\epsilon_x A} \quad (6)$$

where the force ( $F$ ) was measured using TFM, the cross-sectional area ( $A$ ) using optical imaging (width) and ultrasound (height) assuming a rectangular cross-section, and the axial strain ( $\epsilon_x$ ) using ultrasound. The value of  $E$ , based on measurement of  $n = 6$  CMs, was used in the ultrasound force determination calculations using eq 4.

**Mouse Adult Cardiomyocyte Staining.  $\alpha$ -Actinin and Nuclear Staining.** Cells were washed with phosphate-buffered saline with calcium and magnesium (PBS) and fixed in 2% paraformaldehyde for 10 min at room temperature (RT) and then in ice-cold 90% methanol for 10 min. Cells were then permeabilized with 0.5% Triton X-100/0.2% Tween-20 for 30 min at 4 °C and blocked with 5% fetal bovine serum (FBS) for 1 h at RT. Following this, they were incubated with primary mouse anti- $\alpha$ -actinin (Abcam #9465, 1:500), washed with PBS, and then incubated with secondary Alexa Fluor 568-conjugated goat anti-mouse IgG (Invitrogen #A11004, 1:500), both overnight at 4 °C on an orbital platform. Lastly, after rinsing with PBS, cells were incubated with DAPI (Thermo Scientific #62248, 1:5000) for 10 min at RT. Confocal microscopy images were obtained using an Olympus Fluoview 3000 laser scanning confocal microscope (Olympus Corporation). Fluorescence images were acquired using a 40× long working distance objective. For each condition, eight independent images were taken of different groups of cells. Nuclear area and Feret angles were obtained as metrics for nuclear size and orientation, respectively.  $\alpha$ -Actinin content was quantified using ImageJ, by average intensity of  $\alpha$ -actinin divided by the number of nuclei. Sarcomere filaments were automatically detected using ImageJ's integrated ridge detection plugin, and sarcomere length was determined by measuring the distance of intensity peaks between adjacent filaments. The lengths of 20 sarcomeres per cell were acquired and independently averaged. One cell was selected per image, for eight biological replicates per condition. Differences in sarcomere length, nuclear size, and nuclear orientation between cells treated with ultrasound and those not treated (controls) were analyzed by two-tailed Student's *t* test. Equality of variance was tested using the F-test.  $p > 0.05$  was considered nonsignificant for all statistical tests.

**Live/Dead and Nuclear Staining.** Cells were washed with PBS and incubated with 6  $\mu$ M calcein AM and 4  $\mu$ M ethidium homodimer-1 prepared from the LIVE/DEAD viability/cytotoxicity kit (Invitrogen #L3224) for 30 min at 37 °C. The cells were then washed with PBS and incubated with Hoechst counterstain (Thermo Scientific #62249, 1:2500) for 10 min at 37 °C. Confocal images were acquired using a 10× 0.40 NA objective lens. For each condition, five independent images were taken of different groups of cells. Cells positive for both green “live” cytoplasmic stain and blue nuclear stain were counted as live cells. Red nuclei were counted as dead cells. Green cytoplasm and red nuclei were noted to be mutually exclusive. Percent live cells was determined by dividing the live cell count by the total (live + dead) cell count for each image. The difference in percent live cells between cells treated with ultrasound and those not treated (controls) was analyzed by two-tailed Student's *t* test. Equality of variance was tested using the F-test.  $p > 0.05$  was considered nonsignificant

**3D Biowire Microtissue Staining.** Biowire tissues were fixed in 4% paraformaldehyde overnight, permeabilized with 0.2% Tween 20 for 1 h, and then blocked for 1 h with 10% FBS, all at 4 °C. They were then incubated with primary mouse anti- $\alpha$ -actinin (Abcam #9465, 1:200), washed with PBS, and incubated with secondary Alexa Fluor 568-conjugated goat anti-mouse IgG (Invitrogen #A11004, 1:200), each overnight at 4 °C on an orbital platform (note that the washing step was also overnight). Tissues were then rinsed with PBS and incubated with DAPI stain (Thermo Scientific #62248, 1:5000) for 15 min at RT. Confocal images were acquired using a 40× long working distance objective at three independent positions along the long axis of microtissues subjected to ultrasound or not (controls).  $\alpha$ -Actinin

content was quantified using ImageJ, by average intensity of  $\alpha$ -actinin divided by the number of nuclei. Nuclear area and Feret angles were measured as metrics for nuclear size and orientation. Differences between Biowires treated with ultrasound and those not treated (controls) were analyzed by two-tailed Student's *t* test. Equality of variance was tested using the F-test.  $p > 0.05$  was considered nonsignificant for all statistical tests.

**Cardiac Spheroid Staining.** Spheroids were collected, washed with PBS, and fixed in 4% paraformaldehyde for 20 min at RT. They were then permeabilized with 0.1% Triton X-100 for 4 min, washed with PBS, and blocked with 5% FBS/2% bovine serum albumin (BSA) for 1 h, both at RT. Spheroids were then incubated with primary mouse anti- $\alpha$ -actinin (Abcam #9465, 1:200) overnight at 4 °C, washed, incubated with secondary Alexa Fluor 568-conjugated goat anti-mouse IgG (Invitrogen #A11004, 1:200) for 90 min at RT, washed, and incubated with DAPI stain (Thermo Scientific #62248, 1:5000) for 4 min at RT. Individual spheroids were suspended in PBS droplets on glass slides, and confocal microscopy images were obtained using a 10× 0.4 NA objective. For each condition, three independent images were taken of different spheroids to generate three biological replicates.  $\alpha$ -Actinin content was quantified using ImageJ, by average intensity of  $\alpha$ -actinin divided by the number of nuclei. Nuclear area and Feret angles were measured as metrics for nuclear size and orientation. Differences between spheroids imaged with ultrasound vs those not (controls) were analyzed by two-tailed Student's *t* test. Equality of variance was tested using the F-test.  $p > 0.05$  was considered nonsignificant for all statistical tests.

**Human Cardiac Microvascular Endothelial Cell Staining.** Cells were washed with PBS, fixed in 4% paraformaldehyde for 15 min, and permeabilized with 0.1% Triton X-100 for 5 min, both at RT. They were then blocked with 3% BSA for 30 min at 37 °C. Following this, the cells were incubated with primary rabbit anti-VE-cadherin (Abcam #33168, 1:300) overnight at 4 °C, washed, incubated with secondary Alexa Fluor 488-conjugated goat anti-rabbit IgG (Invitrogen #A11008, 1:200) for 1 h at RT, washed, and incubated with DAPI stain (Thermo Scientific #62248, 1:5000) for 5 min at RT. Confocal microscopy Z-stacks were obtained using a 40× long working distance objective (Olympus Life Science) and processed as maximum intensity projections using ImageJ.

## ASSOCIATED CONTENT

### Supporting Information

The Supporting Information is available free of charge at <https://pubs.acs.org/doi/10.1021/acsnano.3c06325>.

Figures of ultrasound measurements of the change in height of a beating cardiomyocyte along its length and immunofluorescence image of cardiac microtissue cross-section ([PDF](#))

Supplemental Video 1: adult mouse cardiomyocyte optical image and ultrasound tracing ([MP4](#))

Supplemental Video 2: cardiac spheroid optical image and ultrasound tracing ([MP4](#))

Supplemental Video 3: immature cardiac spheroid ultrasound tracing ([MP4](#))

Supplemental Video 4: cardiac microtissue ultrasound tracing ([MP4](#))

## AUTHOR INFORMATION

### Corresponding Authors

Eric M. Strohm — Department of Mechanical and Industrial Engineering, University of Toronto, Toronto MSS 3G8, Canada; Translational Biology and Engineering Program, Ted Rogers Center for Heart Research, Toronto MSG 1M1, Canada; Email: [estrohm@torontomu.ca](mailto:estrohm@torontomu.ca)

Craig A. Simmons — Department of Mechanical and Industrial Engineering, University of Toronto, Toronto MSS

3G8, Canada; Translational Biology and Engineering Program, Ted Rogers Center for Heart Research, Toronto MSG 1M1, Canada; Institute of Biomedical Engineering, University of Toronto, Toronto MSS 3G9, Canada; Email: [csimmons@utoronto.ca](mailto:csimmons@utoronto.ca)

### Authors

Neal I. Callaghan — Translational Biology and Engineering Program, Ted Rogers Center for Heart Research, Toronto MSG 1M1, Canada; Institute of Biomedical Engineering, University of Toronto, Toronto MSS 3G9, Canada

Yu Ding — Translational Biology and Engineering Program, Ted Rogers Center for Heart Research, Toronto MSG 1M1, Canada; Institute of Biomedical Engineering, University of Toronto, Toronto MSS 3G9, Canada

Neda Latifi — Department of Mechanical and Industrial Engineering, University of Toronto, Toronto MSS 3G8, Canada; Translational Biology and Engineering Program, Ted Rogers Center for Heart Research, Toronto MSG 1M1, Canada

Naimeh Rafatian — Toronto General Hospital Research Institute, Toronto MSG 2C4, Canada

Shunsuke Funakoshi — McEwen Stem Cell Institute, University Health Network, Toronto MSG 1L7, Canada

Ian Fernandes — McEwen Stem Cell Institute, University Health Network, Toronto MSG 1L7, Canada

Cristine J. Reitz — Translational Biology and Engineering Program, Ted Rogers Center for Heart Research, Toronto MSG 1M1, Canada; Department of Physiology, University of Toronto, Toronto MSS 1A8, Canada; [orcid.org/0000-0002-1748-0501](https://orcid.org/0000-0002-1748-0501)

Michelle Di Paola — Translational Biology and Engineering Program, Ted Rogers Center for Heart Research, Toronto MSG 1M1, Canada; Department of Physiology, University of Toronto, Toronto MSS 1A8, Canada

Anthony O. Gramolini — Translational Biology and Engineering Program, Ted Rogers Center for Heart Research, Toronto MSG 1M1, Canada; Department of Physiology, University of Toronto, Toronto MSS 1A8, Canada; [orcid.org/0000-0003-1109-2070](https://orcid.org/0000-0003-1109-2070)

Milica Radisic — Institute of Biomedical Engineering, University of Toronto, Toronto MSS 3G9, Canada; Toronto General Hospital Research Institute, Toronto MSG 2C4, Canada; Department of Chemical Engineering and Applied Chemistry, University of Toronto, Toronto MSS 3E5, Canada; [orcid.org/0000-0003-1249-4135](https://orcid.org/0000-0003-1249-4135)

Gordon Keller — McEwen Stem Cell Institute, University Health Network, Toronto MSG 1L7, Canada; Department of Medical Biophysics, University of Toronto, Toronto MSG 1L7, Canada

Michael C. Kolios — Department of Physics, Toronto Metropolitan University, Toronto MSB 2K3, Canada; [orcid.org/0000-0002-9994-8293](https://orcid.org/0000-0002-9994-8293)

Complete contact information is available at:

<https://pubs.acs.org/doi/10.1021/acsnano.3c06325>

### Notes

The authors declare no competing financial interest.

A preprint of an earlier version of this manuscript was posted as Eric M. Strohm; Neal Callaghan; Neda Latifi; Naimeh Rafatian; Shunsuke Funakoshi; Ian Fernandes; Milica Radisic; Gordon Keller; Michael C. Kolios; Craig A. Simmons. Noninvasive quantification of contractile dynamics in cardiac

cells, spheroids and organs-on-a-chip using high frequency ultrasound. 2022.06.28.497094. bioRxiv. <https://www.biorxiv.org/content/10.1101/2022.06.28.497094v1> (accessed December 9, 2023).

## ACKNOWLEDGMENTS

We are grateful to the Collaborative Advanced Microscopy Laboratories (CamiLoD) at the University of Toronto for the use of their atomic force microscope. This study was funded by the Medicine by Design New Ideas Fund (MbDNI-2017-01) and a Collaborative Health Research Program grant from the Natural Science and Engineering Research Council of Canada (NSERC; CHRPJ 5083) and Canadian Institutes of Health Research (CPG-151946). E.S. was supported by an NSERC postdoctoral scholarship and a Medicine by Design Postdoctoral Fellowship. N.I.C. was supported by a C. David Naylor Fellowship Endowed by a Gift from the Arthur L. Irving Foundation, Ontario Graduate Scholarship, NSERC Vanier Canada Graduate Scholarship, and NSERC CREATE TOeP Scholarship. N.L. was supported by an NSERC postdoctoral scholarship and a Fonds de Recherche du Quebec—Nature et Technologies Postdoctoral Fellowship Award. The Table of Contents figure was created with BioRender.com.

## REFERENCES

- (1) Benam, K. H.; Dauth, S.; Hassell, B.; Herland, A.; Jain, A.; Jang, K.-J.; Karalis, K.; Kim, H. J.; MacQueen, L.; Mahmoodian, R.; Musah, S.; Torisawa, Y.; van der Meer, A. D.; Villenave, R.; Yadid, M.; Parker, K. K.; Ingber, D. E. Engineered In Vitro Disease Models. *Annual Review of Pathology: Mechanisms of Disease* **2015**, *10* (1), 195–262.
- (2) Zuppinger, C. 3D Culture for Cardiac Cells. *Biochimica et Biophysica Acta (BBA) - Molecular Cell Research* **2016**, *1863* (7), 1873–1881.
- (3) Ronaldson-Bouchard, K.; Vunjak-Novakovic, G. Organs-on-a-Chip: A Fast Track for Engineered Human Tissues in Drug Development. *Cell Stem Cell* **2018**, *22* (3), 310–324.
- (4) Zhang, B.; Korolj, A.; Lai, B. F. L.; Radisic, M. Advances in Organ-on-a-Chip Engineering. *Nature Reviews Materials* **2018**, *3* (8), 257–278.
- (5) Wang, E. Y.; Rafatian, N.; Zhao, Y.; Lee, A.; Lai, B. F. L.; Lu, R. X.; Jekic, D.; Davenport Huyer, L.; Knee-Walden, E. J.; Bhattacharya, S.; Backx, P. H.; Radisic, M. Biowire Model of Interstitial and Focal Cardiac Fibrosis. *ACS Cent. Sci.* **2019**, *5* (7), 1146–1158.
- (6) Zhao, Y.; Rafatian, N.; Wang, E. Y.; Feric, N. T.; Lai, B. F. L.; Knee-Walden, E. J.; Backx, P. H.; Radisic, M. Engineering Microenvironment for Human Cardiac Tissue Assembly in Heart-on-a-Chip Platform. *Matrix Biology* **2020**, 85–86, 189–204.
- (7) Mummery, C. L.; Zhang, J.; Ng, E. S.; Elliott, D. A.; Elefanty, A. G.; Kamp, T. J. Differentiation of Human Embryonic Stem Cells and Induced Pluripotent Stem Cells to Cardiomyocytes. *Circ. Res.* **2012**, *111* (3), 344–358.
- (8) Tzatzalos, E.; Abilez, O. J.; Shukla, P.; Wu, J. C. Engineered Heart Tissues and Induced Pluripotent Stem Cells: Macro- and Microstructures for Disease Modeling, Drug Screening, and Translational Studies. *Adv. Drug Delivery Rev.* **2016**, *96*, 234–244.
- (9) del Alamo, J. C.; Lemons, D.; Serrano, R.; Savchenko, A.; Cerignoli, F.; Bodmer, R.; Mercola, M. High Throughput Physiological Screening of iPSC-Derived Cardiomyocytes for Drug Development. *Biochimica et Biophysica Acta (BBA) - Molecular Cell Research* **2016**, *1863* (7), 1717–1727.
- (10) Savoji, H.; Mohammadi, M. H.; Rafatian, N.; Toroghi, M. K.; Wang, E. Y.; Zhao, Y.; Korolj, A.; Ahadian, S.; Radisic, M. Cardiovascular Disease Models: A Game Changing Paradigm in Drug Discovery and Screening. *Biomaterials* **2019**, *198*, 3–26.
- (11) Xi, B.; Wang, T.; Li, N.; Ouyang, W.; Zhang, W.; Wu, J.; Xu, X.; Wang, X.; Abassi, Y. A. Functional Cardiotoxicity Profiling and Screening Using the xCELLigence RTCA Cardio System. *Journal of Laboratory Automation* **2011**, *16* (6), 415–421.
- (12) Liu, J.; Sun, N.; Bruce, M. A.; Wu, J. C.; Butte, M. J. Atomic Force Mechanobiology of Pluripotent Stem Cell-Derived Cardiomyocytes. *PLoS One* **2012**, *7* (5), No. e37559.
- (13) Kajzar, A.; Cesa, C. M.; Kirchgessner, N.; Hoffmann, B.; Merkel, R. Toward Physiological Conditions for Cell Analyses: Forces of Heart Muscle Cells Suspended Between Elastic Micropillars. *Biophys. J.* **2008**, *94* (5), 1854–1866.
- (14) Beussman, K. M.; Rodriguez, M. L.; Leonard, A.; Taparia, N.; Thompson, C. R.; Sniadecki, N. J. Micropost Arrays for Measuring Stem Cell-Derived Cardiomyocyte Contractility. *Methods* **2016**, *94*, 43–50.
- (15) Kim, K.; Taylor, R.; Sim, J. Y.; Park, J.; Norman, J.; Fajardo, G.; Bernstein, D.; Pruitt, B. L. Calibrated Micropost Arrays for Biomechanical Characterisation of Cardiomyocytes. *IET Micro Nano Letters* **2011**, *6* (5), 317–322.
- (16) Rodriguez, M. L.; Graham, B. T.; Pabon, L. M.; Han, S. J.; Murry, C. E.; Sniadecki, N. J. Measuring the Contractile Forces of Human Induced Pluripotent Stem Cell-Derived Cardiomyocytes With Arrays of Microposts. *J. Biomech Eng.* **2014**, *136* (S), 051005–051005.
- (17) Grosberg, A.; Nesmith, A. P.; Goss, J. A.; Brigham, M. D.; McCain, M. L.; Parker, K. K. Muscle on a Chip: In Vitro Contractility Assays for Smooth and Striated Muscle. *Journal of Pharmacological and Toxicological Methods* **2012**, *65* (3), 126–135.
- (18) Feinberg, A. W.; Feigel, A.; Shevkoplyas, S. S.; Sheehy, S.; Whitesides, G. M.; Parker, K. K. Muscular Thin Films for Building Actuators and Powering Devices. *Science* **2007**, *317* (5843), 1366–1370.
- (19) Sheehy, S. P.; Pasqualini, F.; Grosberg, A.; Park, S. J.; Aratyn-Schaus, Y.; Parker, K. K. Quality Metrics for Stem Cell-Derived Cardiac Myocytes. *Stem Cell Reports* **2014**, *2* (3), 282–294.
- (20) Hume, S. Development of a Novel Device for High-throughput Screening of Cell Contraction. Master's Thesis, University of Toronto. 2014.
- (21) Banerjee, I.; Carrion, K.; Serrano, R.; Dyo, J.; Sasik, R.; Lund, S.; Willem, E.; Aceves, S.; Meili, R.; Mercola, M.; Chen, J.; Zambon, A.; Hardiman, G.; Doherty, T. A.; Lange, S.; del Alamo, J. C.; Nigam, V. Cyclic Stretch of Embryonic Cardiomyocytes Increases Proliferation, Growth, and Expression While Repressing Tgf- $\beta$  Signaling. *Journal of Molecular and Cellular Cardiology* **2015**, *79*, 133–144.
- (22) Tseng, Q.; Duchemin-Pelletier, E.; Deshiere, A.; Balland, M.; Guillou, H.; Filhol, O.; Thery, M. Spatial Organization of the Extracellular Matrix Regulates Cell-Cell Junction Positioning. *Proc. Natl. Acad. Sci. U. S. A.* **2012**, *109* (5), 1506–1511.
- (23) MacQueen, L.; Chebotarev, O.; Simmons, C. A.; Sun, Y. Miniaturized Platform with On-Chip Strain Sensors for Compression Testing of Arrayed Materials. *Lab Chip* **2012**, *12* (20), 4178–4184.
- (24) Hansen, K. J.; Favreau, J. T.; Gershkoff, J. R.; Laflamme, M. A.; Albrecht, D. R.; Gaudette, G. R. Optical Method to Quantify Mechanical Contraction and Calcium Transients of Human Pluripotent Stem Cell-Derived Cardiomyocytes. *Tissue Engineering Part C: Methods* **2017**, *23* (8), 445–454.
- (25) Zimmermann, W.-H.; Schneiderbanger, K.; Schubert, P.; Didié, M.; Müntzel, F.; Heubach, J. F.; Kostin, S.; Neuhaber, W. L.; Eschenhagen, T. Tissue Engineering of a Differentiated Cardiac Muscle Construct. *Circ. Res.* **2002**, *90* (2), 223–230.
- (26) Hansen, A.; Eder, A.; Bönstrup, M.; Flato, M.; Mewe, M.; Schaaf, S.; Aksehirlioglu, B.; Schwörer, A.; Uebeler, J.; Eschenhagen, T. Development of a Drug Screening Platform Based on Engineered Heart Tissue. *Circ. Res.* **2010**, *107* (1), 35–44.
- (27) Boudou, T.; Legant, W. R.; Mu, A.; Borochin, M. A.; Thavandiran, N.; Radisic, M.; Zandstra, P. W.; Epstein, J. A.; Margulies, K. B.; Chen, C. S. A Microfabricated Platform to Measure and Manipulate the Mechanics of Engineered Cardiac Microtissues. *Tissue Engineering Part A* **2012**, *18* (9–10), 910–919.

- (28) Nunes, S. S.; Miklas, J. W.; Liu, J.; Aschar-Sobbi, R.; Xiao, Y.; Zhang, B.; Jiang, J.; Massé, S.; Gagliardi, M.; Hsieh, A.; Thavandiran, N.; Laflamme, M. A.; Nanthakumar, K.; Gross, G. J.; Backx, P. H.; Keller, G.; Radisic, M. Biowire: A Platform for Maturation of Human Pluripotent Stem Cell-Derived Cardiomyocytes. *Nat. Meth.* **2013**, *10* (8), 781–787.
- (29) Krishnamoorthy, V. K.; Sengupta, P. P.; Gentile, F.; Khandheria, B. K. History of Echocardiography and Its Future Applications in Medicine. *Crit. Care Med.* **2007**, *35* (8), S309–S313.
- (30) Meyer, R. A. History of Ultrasound in Cardiology. *JUM* **2004**, *23* (1), 1–11.
- (31) Kaul, S.; Miller, J. G.; Grayburn, P. A.; Hashimoto, S.; Hibberd, M.; Holland, M. R.; Houle, H. C.; Klein, A. L.; Knoll, P.; Lang, R. M.; Lindner, J. R.; McCulloch, M. L.; Metz, S.; Mor-Avi, V.; Pearlman, A. S.; Pellikka, P. A.; DeMars Plambeck, N.; Prater, D.; Porter, T. R.; Sahn, D. J.; Thomas, J. D.; Thomenius, K. E.; Weissman, N. J. A Suggested Roadmap for Cardiovascular Ultrasound Research for the Future. *Journal of the American Society of Echocardiography* **2011**, *24* (4), 455–464.
- (32) Zhao, Y.; Rafatian, N.; Wang, E. Y.; Feric, N. T.; Lai, B. F. L.; Knee-Walden, E. J.; Backx, P. H.; Radisic, M. Engineering Microenvironment for Human Cardiac Tissue Assembly in Heart-on-a-Chip Platform. *Matrix Biology* **2020**, *85–86*, 189–204.
- (33) Chandraratna, P. A. N.; Choudhary, S.; Jones, J. P.; Chandrasoma, P.; Kapoor, A.; Gallet, J. Visualization of Myocardial Cellular Architecture Using Acoustic Microscopy. *American Heart Journal* **1992**, *124* (5), 1358–1364.
- (34) Sajio, Y.; Tanaka, M.; Okawai, H.; Sasaki, H.; Nitta, S.-I.; Dunn, F. Ultrasonic Tissue Characterization of Infarcted Myocardium by Scanning Acoustic Microscopy. *Ultrasound in Medicine & Biology* **1997**, *23* (1), 77–85.
- (35) Masugata, H.; et al. Relationship between Myocardial Tissue Density Measured by Microgravimetry and Sound Speed Measured by Acoustic Microscopy. *Ultrasound in Medicine & Biology* **1999**, *25* (9), 1459–1463.
- (36) Funakoshi, S.; Fernandes, I.; Mastikhina, O.; Wilkinson, D.; Tran, T.; Dhahri, W.; Mazine, A.; Yang, D.; Burnett, B.; Lee, J.; Protze, S.; Bader, G. D.; Nunes, S. S.; Laflamme, M.; Keller, G. Generation of Mature Compact Ventricular Cardiomyocytes from Human Pluripotent Stem Cells. *Nat. Commun.* **2021**, *12* (1), 3155.
- (37) Ackers-Johnson, M.; Li, P. Y.; Holmes, A. P.; O'Brien, S.-M.; Pavlovic, D.; Foo, R. S. A Simplified, Langendorff-Free Method for Concomitant Isolation of Viable Cardiac Myocytes and Nonmyocytes From the Adult Mouse Heart Novelty and Significance. *Circ. Res.* **2016**, *119* (8), 909–920.
- (38) Ribeiro, A. J. S.; Ang, Y.-S.; Fu, J.-D.; Rivas, R. N.; Mohamed, T. M. A.; Higgs, G. C.; Srivastava, D.; Pruitt, B. L. Contractility of Single Cardiomyocytes Differentiated from Pluripotent Stem Cells Depends on Physiological Shape and Substrate Stiffness. *Proc. Natl. Acad. Sci. U.S.A.* **2015**, *112* (41), 12705–12710.
- (39) Cordelires, F. Manual Tracking. <https://imagej.nih.gov/ij/plugins/manual-tracking.html> (accessed 2020-09-04).
- (40) Chopra, A.; Tabdanov, E.; Patel, H.; Janmey, P. A.; Kresh, J. Y. Cardiac Myocyte Remodeling Mediated by N-Cadherin-Dependent Mechanosensing. *American Journal of Physiology-Heart and Circulatory Physiology* **2011**, *300* (4), H1252–H1266.
- (41) Toepfer, C. N.; Sharma, A.; Cicconet, M.; Garfinkel, A. C.; Mücke, M.; Neyazi, M.; Willcox, J. A. L.; Agarwal, R.; Schmid, M.; Rao, J.; Ewoldt, J.; Pourquié, O.; Chopra, A.; Chen, C. S.; Seidman, J. G.; Seidman, C. E. SarcTrack: An Adaptable Software Tool for Efficient Large-Scale Analysis of Sarcomere Function in hiPSC-Cardiomyocytes. *Circ. Res.* **2019**, *124* (8), 1172–1183.
- (42) Qian, T.; Gil, D. A.; Guzman, E. C.; Gastfriend, B. D.; Tweed, K. E.; Palecek, S. P.; Skala, M. C. Adaptable Pulsatile Flow Generated from Stem Cell-Derived Cardiomyocytes Using Quantitative Imaging-Based Signal Transduction. *Lab Chip* **2020**, *20* (20), 3744–3756.
- (43) Pasqualini, F. S.; Agarwal, A.; O'Connor, B. B.; Liu, Q.; Sheehy, S. P.; Parker, K. K. Traction Force Microscopy of Engineered Cardiac Tissues. *PLoS One* **2018**, *13* (3), No. e0194706.
- (44) Fassina, L.; Assenza, M. R.; Miragoli, M.; Isidori, A. M.; Naro, F.; Barbagallo, F. Cell Shortening and Calcium Homeostasis Analysis in Adult Cardiomyocytes via a New Software Tool. *Biomedicines* **2022**, *10* (3), 640.
- (45) McCain, M. L.; Yuan, H.; Pasqualini, F. S.; Campbell, P. H.; Parker, K. K. Matrix Elasticity Regulates the Optimal Cardiac Myocyte Shape for Contractility. *American Journal of Physiology-Heart and Circulatory Physiology* **2014**, *306* (11), H1525–H1539.
- (46) Wiklund, M. Acoustofluidics 12: Biocompatibility and Cell Viability in Microfluidic Acoustic Resonators. *Lab Chip* **2012**, *12* (11), 2018–2028.
- (47) Baudoin, M.; Thomas, J.-L.; Sahely, R. A.; Gerbedoen, J.-C.; Gong, Z.; Sivery, A.; Matar, O. B.; Smagin, N.; Favreau, P.; Vlandas, A. Spatially Selective Manipulation of Cells with Single-Beam Acoustical Tweezers. *Nat. Commun.* **2020**, *11* (1), 4244.
- (48) Kim, M. G.; Park, J.; Lim, H. G.; Yoon, S.; Lee, C.; Chang, J. H.; Shung, K. K. Label-Free Analysis of the Characteristics of a Single Cell Trapped by Acoustic Tweezers. *Sci. Rep.* **2017**, *7* (1), 14092.
- (49) Lim, H. G.; Shung, K. K. Quantification of Inter-Erythrocyte Forces with Ultra-High Frequency (410 MHz) Single Beam Acoustic Tweezer. *Ann. Biomed Eng.* **2017**, *45* (9), 2174–2183.
- (50) Nishimura, S.; Nagai, S.; Katoh, M.; Yamashita, H.; Saeki, Y.; Okada, J.-i.; Hisada, T.; Nagai, R.; Sugiura, S. Microtubules Modulate the Stiffness of Cardiomyocytes Against Shear Stress. *Circ. Res.* **2006**, *98* (1), 81–87.
- (51) Gupta, S. K.; Li, Y.; Guo, M. Anisotropic Mechanics and Dynamics of a Living Mammalian Cytoplasm. *Soft Matter* **2019**, *15* (2), 190–199.
- (52) Efremov, Y. M.; Velay-Lizancos, M.; Weaver, C. J.; Athamneh, A. I.; Zavattieri, P. D.; Suter, D. M.; Raman, A. Anisotropy vs Isotropy in Living Cell Indentation with AFM. *Sci. Rep.* **2019**, *9* (1), 5757.
- (53) Shaw, J.; Izu, L.; Chen-Izu, Y. Mechanical Analysis of Single Myocyte Contraction in a 3-D Elastic Matrix. *PLoS One* **2013**, *8* (10), No. e75492.
- (54) Caporizzo, M. A.; Chen, C. Y.; Salomon, A. K.; Margulies, K. B.; Prosser, B. L. Microtubules Provide a Viscoelastic Resistance to Myocyte Motion. *Biophys. J.* **2018**, *115* (9), 1796–1807.
- (55) Tseng, Q.; Duchemin-Pelletier, E.; Deshiere, A.; Balland, M.; Guillou, H.; Filhol, O.; Théry, M. Spatial Organization of the Extracellular Matrix Regulates Cell-Cell Junction Positioning. *Proc. Natl. Acad. Sci. U.S.A.* **2012**, *109* (5), 1506–1511.
- (56) Traction Force Microscopy - ImageJ. plugins by Qingzong TSENG. <https://sites.google.com/site/qingzongtseng/tfm> (accessed 2018-10-14).
- (57) Callaghan, N. I.; Lee, S.-H.; Hadipour-Lakmehsari, S.; Lee, X. A.; Ahsan Siraj, M.; Driouchi, A.; Yip, C. M.; Husain, M.; Simmons, C. A.; Gramolini, A. O. Functional Culture and in Vitro Genetic and Small-Molecule Manipulation of Adult Mouse Cardiomyocytes. *Communications Biology* **2020**, *3* (1), 1–10.
- (58) Lin, G.; Palmer, R. E.; Pister, K. S. J.; Roos, K. P. Miniature Heart Cell Force Transducer System Implemented in MEMS Technology. *IEEE Transactions on Biomedical Engineering* **2001**, *48* (9), 996–1006.
- (59) Nishimura, S.; Yasuda, S.; Katoh, M.; Yamada, K. P.; Yamashita, H.; Saeki, Y.; Sunagawa, K.; Nagai, R.; Hisada, T.; Sugiura, S. Single Cell Mechanics of Rat Cardiomyocytes under Isometric, Unloaded, and Physiologically Loaded Conditions. *American Journal of Physiology - Heart and Circulatory Physiology* **2004**, *287* (1), H196–H202.
- (60) Iribe, G.; Helmes, M.; Kohl, P. Force-Length Relations in Isolated Intact Cardiomyocytes Subjected to Dynamic Changes in Mechanical Load. *American Journal of Physiology - Heart and Circulatory Physiology* **2007**, *292* (3), H1487–H1497.
- (61) Yin, S.; Zhang, X.; Zhan, C.; Wu, J.; Xu, J.; Cheung, J. Measuring Single Cardiac Myocyte Contractile Force via Moving a Magnetic Bead. *Biophys. J.* **2005**, *88* (2), 1489–1495.
- (62) Shih, C.-C.; Qian, X.; Ma, T.; Han, Z.; Huang, C.-C.; Zhou, Q.; Shung, K. K. Quantitative Assessment of Thin-Layer Tissue Viscoelastic Properties Using Ultrasonic Micro-Elastography With

- Lamb Wave Model. *IEEE Transactions on Medical Imaging* **2018**, *37* (8), 1887–1898.
- (63) Hong, X.; Annamalai, R. T.; Kemerer, T. S.; Deng, C. X.; Stegemann, J. P. Multimode Ultrasound Viscoelastography for Three-Dimensional Interrogation of Microscale Mechanical Properties in Heterogeneous Biomaterials. *Biomaterials* **2018**, *178*, 11–22.
- (64) Hobson, E. C.; Li, W.; Julian, B. A.; Putnam, A. J.; Stegemann, J. P.; Deng, C. X. Resonant Acoustic Rheometry for Non-Contact Characterization of Viscoelastic Biomaterials. *Biomaterials* **2021**, *269*, 120676.
- (65) Zhao, Y.; Rafatian, N.; Feric, N. T.; Cox, B. J.; Aschar-Sobbi, R.; Wang, E. Y.; Aggarwal, P.; Zhang, B.; Conant, G.; Ronaldson-Bouchard, K.; Pahnke, A.; Protze, S.; Lee, J. H.; Davenport Huyer, L.; Jekic, D.; Wickeler, A.; Naguib, H. E.; Keller, G. M.; Vunjak-Novakovic, G.; Broeckel, U.; Backx, P. H.; Radisic, M. A Platform for Generation of Chamber-Specific Cardiac Tissues and Disease Modeling. *Cell* **2019**, *176* (4), 913–927.
- (66) Mohammadi, H.; Arora, P. D.; Simmons, C. A.; Janmey, P. A.; McCulloch, C. A. Inelastic Behaviour of Collagen Networks in Cell-Matrix Interactions and Mechanosensation. *Journal of The Royal Society Interface* **2015**, *12* (102), 20141074.
- (67) Sebastian, J. A.; Strohm, E. M.; Chérin, E.; Mirani, B.; Démoré, C. E. M.; Kolios, M. C.; Simmons, C. A. High-Frequency Quantitative Ultrasound for the Assessment of the Acoustic Properties of Engineered Tissues in Vitro. *Acta Biomaterialia* **2023**, *157*, 288–296.
- (68) Jackman, C. P.; Carlson, A. L.; Bursac, N. Dynamic Culture Yields Engineered Myocardium with Near-Adult Functional Output. *Biomaterials* **2016**, *111*, 66–79.
- (69) Lian, X.; Hsiao, C.; Wilson, G.; Zhu, K.; Hazeltine, L. B.; Azarin, S. M.; Raval, K. K.; Zhang, J.; Kamp, T. J.; Palecek, S. P. Robust Cardiomyocyte Differentiation from Human Pluripotent Stem Cells via Temporal Modulation of Canonical Wnt Signaling. *Proc. Natl. Acad. Sci. U.S.A.* **2012**, *109* (27), DOI: 10.1073/pnas.1200250109.
- (70) Lian, X.; Zhang, J.; Azarin, S. M.; Zhu, K.; Hazeltine, L. B.; Bao, X.; Hsiao, C.; Kamp, T. J.; Palecek, S. P. Directed Cardiomyocyte Differentiation from Human Pluripotent Stem Cells by Modulating Wnt/β-Catenin Signaling under Fully Defined Conditions. *Nat. Protoc.* **2013**, *8* (1), 162–175.
- (71) Kattman, S. J.; Witty, A. D.; Gagliardi, M.; Dubois, N. C.; Niapour, M.; Hotta, A.; Ellis, J.; Keller, G. Stage-Specific Optimization of Activin/Nodal and BMP Signaling Promotes Cardiac Differentiation of Mouse and Human Pluripotent Stem Cell Lines. *Cell Stem Cell* **2011**, *8* (2), 228–240.
- (72) Edelstein, A.; Amodaj, N.; Hoover, K.; Vale, R.; Stuurman, N. Computer Control of Microscopes Using μManager. *Current Protocols in Molecular Biology* **2010**, *92* (1), 1–17.